ADVANCED FUNCTIONAL MATERIALS
www.afm-journal.de

Sequence–Structure–Property Relationships of Recombinant Spider Silk Proteins: Integration of Biopolymer Design, Processing, and Modeling

Sreevidhya Tarakkad Krishnaji, Graham Bratzel, Michelle E. Kinahan, Jonathan A. Kluge, Cristian Staii, Joyce Y. Wong, Markus J. Buehler,* and David L. Kaplan**

The mechanical properties of spider silks drive interest as sources of new materials. However, there remains a lot to learn regarding the relationships between sequence, structure, and mechanical properties. In order to predict the types of sequence–functional relationships, synthesis–characterization–computation are integrated using recombinant spider silk-like block copolymers. Two designs are studied, both with origins from the spider *Nephila clavipes*. These proteins are studied both experimentally and in silico to understand the relationships between sequence chemistry, processing, structure, and materials function. Films formed from the two proteins are thoroughly characterized. In parallel, molecular modeling is used to assess the propensity of the two sequences to form β-sheets or crystalline structures. The results demonstrate that the modeling predicts the structural differences between the two silk-like polymers and these features can also be related to differences in functional outcomes. With this example of relating sequence design (hydrophobic–hydrophilic domains), experiment (genetic design and synthesis), processing (film and fiber formation) and modeling (predictions of crystallinity), synergy among these methods is demonstrated for predictable material outcomes. This approach offers a robust discovery path when looking towards next generation approaches to targeted materials outcomes.

1. Introduction

Nature has modulated and optimized the properties of natural biopolymers such as silk through evolution and exquisite nanostructure engineering. Silks exhibit extraordinary mechanical properties and can be as tough as Kevlar[1,2] yet as stretchable as rubber, while also biocompatible and biodegradable, and have been used for biomedical applications ranging from tissue engineering[3] to gene[4] or drug delivery.[5] The macroscopic mechanical characteristics of spider silk arise from nanoscale morphology, in particular from the interactions within and between the protein strands. In addition to native silks, genetically engineered variants have been designed with carefully programmed sequences that dictate protein folding and hierarchical organization for tailor-made biomaterials. Despite advances in biotechnology, attempts to utilize structure–property relationships in materials design continue to be hindered by a lack of fundamental understanding of the molecular details that govern these relationships, and non-native processing methods cannot rival the material performance of natural systems.

In addition to sequence alterations, control of processing parameters allows for another dimension of material design. Precise control of nano- and microstructure formation has been identified as an important factor in polymeric material features. We have previously reported a unique microfluidic approach to fabricate silk fibers with controllable properties from regenerated silk fibroin solutions.[6] This technique mimics natural silk spinning and allows precise yet tunable control of processing parameters to fabricate fibers for potential applications ranging from tissue engineering to optics.[7,8] Additionally, since the hierarchical organization of silk fibers is closely tied to the extraordinary properties of these materials, the ability to "spin" silks or other biopolymers into fibrous structures is useful to further the understanding of the natural assembly process, and this insight can be applied to the design of new silk-like biopolymers. Unlike bulk processes such as wet-spinning or electrospinning, our method facilitates the rapid fabrication of fibers from small volumes (50 μL).

S. T. Krishnaji, J. A. Kluge, Prof. D. L. Kaplan
Departments of Chemistry & Biomedical Engineering
Tufts University
Medford, MA 02155, USA
E-mail: david.kaplan@tufts.edu
G. Bratzel, Prof. M. J. Buehler
Laboratory for Atomistic and Molecular Mechanics
Department of Civil and Environmental Engineering
Massachusetts Institute of Technology
Cambridge, MA 02139, USA
E-mail: mbuehler@mit.edu
M. E. Kinahan, Prof. J. Y. Wong
Department of Biomedical Engineering
Boston University
Boston, MA 02215, USA
E-mail: jywong@bu.edu
Prof. C. Staii
Department of Physics & Astronomy
Tufts University
Medford, MA 02155, USA

DOI: 10.1002/adfm.201200510

Recent computational approaches have proven useful in advancing the understanding of native silk processing and further elucidating fundamental relationships. Recent studies revealed that β-sheet crystals play a key role in defining the mechanical properties of silks by providing stiff, physically cross-linked domains embedded in a semiamorphous Gly-rich matrix.[9–14] Studies have also shown that the hydration level and solvent conditions, such as ion content and pH, play a significant role in the structure and mechanical properties of silk proteins,[15,16] as well as the transition from concentrated protein dope in the spinning duct to the final spun fiber. The cross-linked β-sheet crystals employ a dense network of hydrogen bonds,[9,11] have dimensions of a few nanometers, and constitute at least 10–15% of the silk volume. The existence of 3_{10} helices and β-turns or β-spirals has been suggested for the less crystalline domains.[10,12,13,17,18] Studies of silk using replica exchange molecular dynamics (REMD)[9,14] have yielded results to compare with experimental structure identification methods.[10,19,20] Other recent computational studies have begun to characterize the mechanics of near-native predictions of MaSp1 proteins.[14] However, owing to the lack of current large-scale atomistic models, the links between peptide sequences of natural silk proteins remains poorly understood.

Spider silks consist of highly repetitive amino acid motifs flanked by non-repetitive N- and C-terminal domains.[21–23] For this study, sequences obtained from major ampullate spidroin 1 (MaSp1) derived from the golden orb–weaving spider *Nephila clavipes* served as our template. This protein is composed of hydrophilic tripeptide motifs, GGX (X = R, L, Y, Q), alternating with polyalanine (hydrophobic) motifs. Amphiphilic silk-like block copolymers were designed from two representative domains, the A domain consisting of a poly–alanine sequence responsible for the formation of rigid, crystalline β-sheets[10] due to intermolecular hydrogen bonding and hydrophobic interactions[24] and the B domain consisting of soft segments of tripeptides of GGX repeats that adopt an alpha helix conformation, providing elasticity to the materials. We have previously reported the design, fabrication and self–assembly of a family of bioengineered spider silk-like block copolymers composed of different repeating units of A and B domains which exhibited different phase behavior in aqueous solution,[25–27] Because of the hydrophilic and hydrophobic nature of the blocks, these materials tend to self-assemble to form periodic nanostructures,[27] indicating the wide range of material properties that can be obtained from a simple set of building blocks.

The main goal of this work was to combine controlled synthesis (genetically programmed), tailorable processing (via controlled microfluidic flow focusing and film assembly) and molecular modeling in a synergistic and cost-effective manner to enable the prediction of functional properties for materials, with specific spider silk-like designs as the target materials. Our objective was to understand the interplay between the primary sequence of building blocks, processing, and assembly in silico using modeling, to further understand relationships between sequence, structure and mechanical characteristics. To this end, two genetic variants were considered: HBA_3 and HAB_3, primarily because of equal numbers of repeats of domains (blocks) and similar molecular weights. The presence of a hexahistidine fusion tag along with a short linker sequence was introduced to enable facile purification.

2. Results and Discussion

2.1 Films and Fiber Formation

Films were fabricated from recombinant silk-like block copolymers (HBA_3, HAB_3). The materials allowed for easy handling and imaging. The thickness of the film can be controlled by concentration of the employed protein solution (data not shown). The films in this study had thickness of 50 μm.

Using a microfluidic channel, fibers were spun from hydrodynamic focusing of the silk-like block copolymers. Initial attempts to spin pure, 8% (w/v, in water) copolymer solutions were not successful (no solid material was observed) most likely because of the length of the peptides, which are considerably shorter than native silks. Protein size as well as prevalence of chain end defects greatly affects the ability to self–assemble into fibers, and the resulting mechanical strength. By mixing the copolymers with regenerated silk (RSF) at a ratio of 70% silk-like copolymer and 30% RSF solution (by weight), we were able to observe production of solid materials for both HAB_3 and HBA_3. SDS-PAGE gel results (Figure SI1, Supporting Information) verify that significant amounts of the copolymers are present in the resultant materials. These materials were imaged via brightfield microscopy as well as higher magnification imaging via SEM (**Figure 1**).

The ability to spin fibers from recombinant silk-like proteins is important for a variety of reasons. Fibers are useful for many applications, and mimicking or exceeding the natural structure and properties has been a goal of silk engineering for many years. Monitoring silk assembly processes- both regenerated and recombinant- would be insightful to the understanding of native silk processing which is not yet fully understood. Additionally, the ability to process recombinant variants via this well-characterized microfluidic technique would be beneficial for screening potential sequences for any material design.

Macroscale imaging illustrates differences between the materials formed from the two copolymer types. Pure RSF and HAB_3 copolymer blends formed fibers with consistent diameters on the order of that of native silk fibers (Figure 1a,b). HBA_3 copolymer blends on the other hand formed some fibrils but also a large amount of non-fibrillar solid material (this combination material will be referred to as non-fibrillar for simplicity). SEM images of the copolymer blend fibers illustrated that the HAB_3 fibers were composed of multiple fibrils and images of the material surfaces illustrate morphological differences between the two copolymer types. HAB_3 blends were much easier to spin, had fewer issues with precipitation and other clogging occurrences, and the resulting fibers behaved similarly to pure RSF fibers in that they were robust and easy to handle and transfer from dry to wet states or from one solution to another. HBA_3 however was more difficult to spin, with the product containing many fiber segments or silk pieces or precipitate rather than a continuous fiber strand. Additionally, this material was markedly more difficult to manipulate or transfer. These spinning experiments demonstrate the differences between the two copolymer types due to sequence variation, as well as how material behavior is affected by processing conditions (fibers vs. films discussed in later sections).

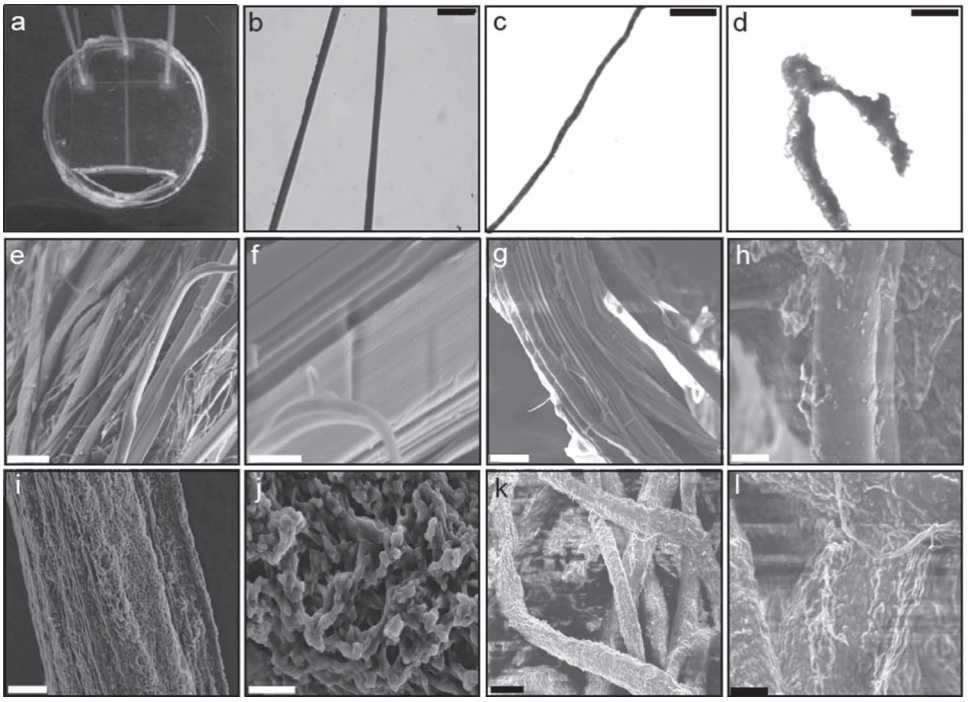

Figure 1. A) Fibers were spun from regenerated silk fibroin (RSF) and mixtures of RSF with HAB_3 and HBA_3 (30% RSF/ 70% copolymer, by weight) using a previously reported microfluidic approach. Brightfield images show B) RSF (scale bar 150 μm), C) RSF/HAB_3 blend (scale bar 150 μm), and D) RSF/HBA_3 blend (scale bar 150 μm) fibers. E–L) SEM images of fibers at varying magnifications to illustrate fiber formation as well as surface properties. E) Native silk, scale bar 30 μm. F) Native silk, scale bar 2 μm. G) RSF fibers, scale bar 8 μm. H) RSF fibers, scale bar 4 μm. I) RSF/ HAB_3 blend, scale bar 30 μm. J) RSF/ HAB_3 blend, scale bar 2 μm. K) RSF/ HBA_3 blend, scale bar 20 μm. L) RSF/ HBA_3 blend, scale bar 5 μm.

2.2. Secondary Structure Analysis of Films andFibers

Films and fibers prepared from recombinant spider silk-like proteins were assessed for differences in the secondary structure by Fourier transform infrared attenuated total reflection (FTIR-ATR) spectroscopy (**Figure 2**). Infrared spectral region within 1700–1500 cm^{-1} was assigned to absorption by peptide backbones of amide I (1700–1600 cm^{-1}) and amide II (1600–1500 cm^{-1}) regions, and has been commonly used for the analysis of different secondary structures of silk. In the present study, single peak positions were considered for each secondary structure.[28] Characteristic assignments of distinct peaks for spider silk were considered in accordance with earlier reports,[29] and single peaks corresponding to the different structures were used for calculation of the fraction of secondary structure. Peaks in the region 1618–1630 cm^{-1} were attributed to β-sheets, whereas 1630–1642 cm^{-1} corresponded to random coil, 1658–1666 cm^{-1} represented α-helices and 1668–1696 cm^{-1} corresponded to β-turns. The secondary structures of the films and fibers were further characterized by deconvolution of IR spectra.

For both films and fibers, differences in secondary structure were observed as shown in Figure 2 (marked in black line). For films, a pronounced peak representing β-sheet was present centered at 1624 ± 2 cm^{-1} for HBA_3 in comparison to HAB_3. HBA_3 showed a strong peak at 1624 ± 2 cm^{-1}, corresponding to β-sheet, along with distinct peaks at 1649 ± 2 cm^{-1} and 1662 ± 2 cm^{-1} representative of random coils and alpha helix, respectively. As for HAB_3, there was only a shoulder at 1624 ± 2 cm^{-1}, along with prominent peaks for random coil and alpha helix.

The relative ratios of different secondary structures were calculated in the amide I region and summarized in **Table 1**. Films made of HBA_3 and HAB_3 were comprised of nearly equal amounts of random coil and alpha helix, but showed a distinct difference in β-sheet content (21.1% vs. 10.8%) respectively. Similar treatment of silk obtained from *Bombyx mori* cast into films using different processing conditions[30] and after Fourier self-deconvolution revealed similar percentages of β-sheet though the repetitive sequences are completely different between the species. The presence of polyalanine residues in block A play an important role in β-sheet formation, as shown previously.[25,26,28] The increased amounts of β-sheet content in HBA_3 is likely due to the sequence chemistry in the hydrophobic block A. An increase in the number of polyalanine blocks promotes the formation of stacks of β-sheet crystallites, thereby decreasing the distance in alanine residues leading to an increase in strength of these newly formed interactions. Thus, HBA_3 has hydrophobic interactions interlocking adjacent chains to stabilize β-sheets, while HAB_3, comprising more repeats of the GGX motif, are unable to form such interactions.

As for the copolymer blend spinning, HAB_3 copolymer blend fibers were composed of 14.6% β-sheets, and their HBA_3 counterparts were 29.9% β-sheets.

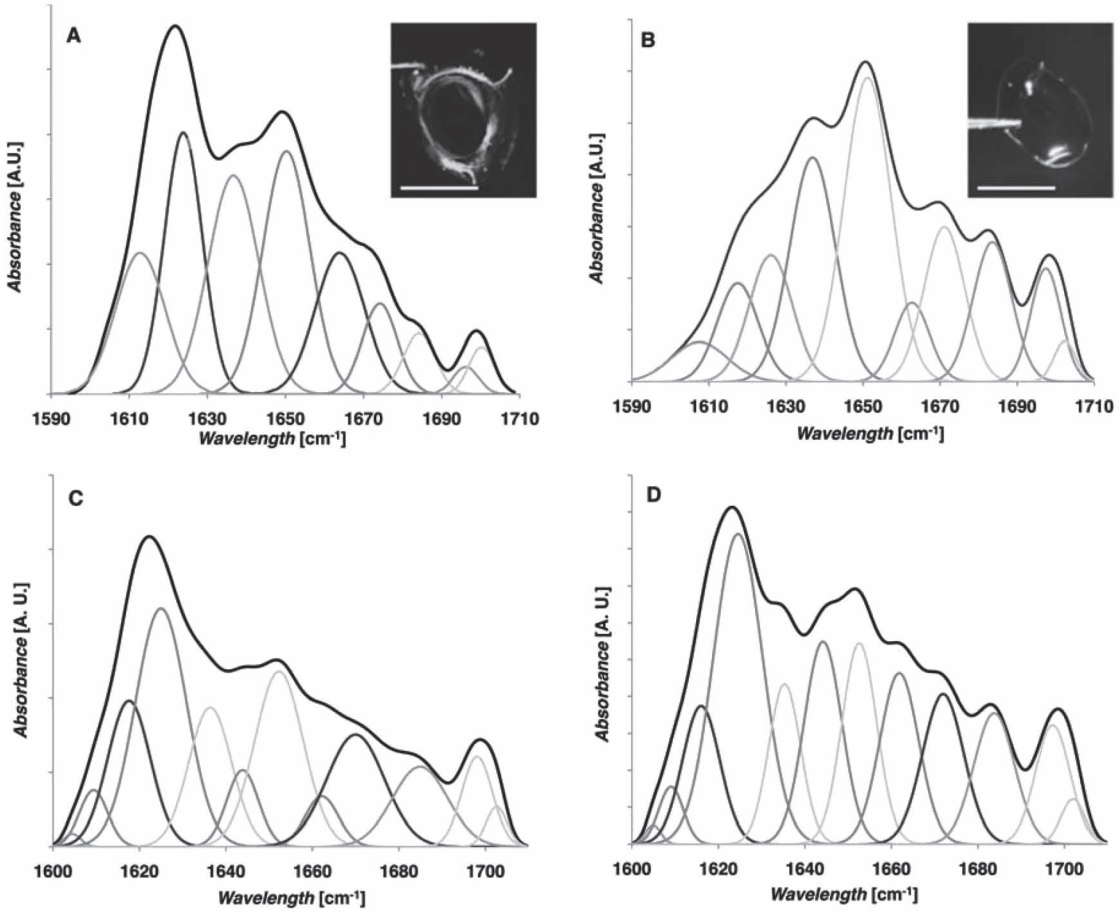

Figure 2. Secondary structure of recombinant silk-like block copolymers. Selected FTIR absorbance spectra of A) HBA_3 film, B) HAB_3 film, C) doped HBA_3/RSF fibers, and D) doped HAB_3/RSF fibers deduced after Fourier self deconvolution. Thick black line represents the original spectra and grey lines represent contributions after deconvolution of the amide I bands. Insets in (A,B) indicate images of respective recombinant spider silk-like proteins formed into films. Scale bars represent 1 cm.

2.3. Structural Features

HBA_3 and HAB_3 films had uniform thickness when analyzed by SEM. At higher magnification, HBA_3 had a wavy-like pattern, while HAB_3 appeared to be relatively smooth (**Figure 3**). Surface features were different for the recombinant protein films due to inter- or intramolecular interaction between blocks during self-assembly. The presence of polyalanine repeats in HBA_3 directed hydrophobic interactions by forming β-sheets.

Table 1. Percentage of secondary structure content of A) silk-like block copolymer films and B) silk-like block copolymer/RSF blended fibers after Fourier self-deconvolution.

Code	Beta sheet	Turn	Alpha helix	Random coil
		A) Films		
HBA_3	21.1 ± 5	24.8 ± 3	13.2 ± 5	12.6 ± 5
HAB_3	10.8 ± 3	27.4 ± 5	8.7 ± 4	11.8 ± 5
		B) Fibers		
HBA_3+RSF	29.9 ± 2	27.1 ± 5	6.3 ± 2	14.3 ± 6
HAB_3+RSF	14.6 ± 5	17.2 ± 5	9.3 ± 3	20.2 ± 4

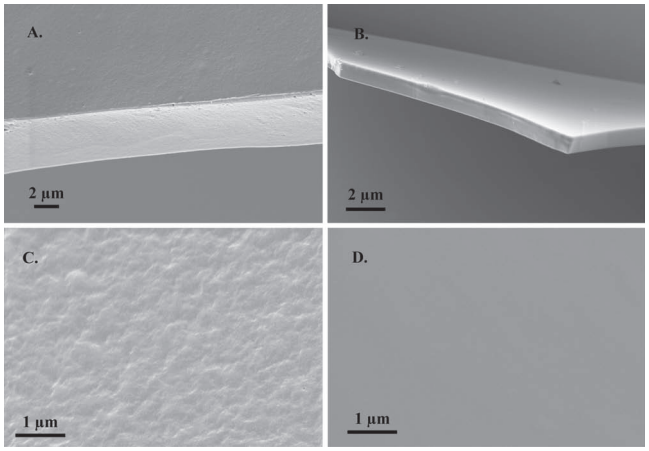

Figure 3. SEM images of A,C) HBA_3 and B,D) HAB_3. Films were observed from edges (A,C) to indicate uniform thickness and overall surface characteristics on the surface of the film was observed from the top face as indicated (B,D).

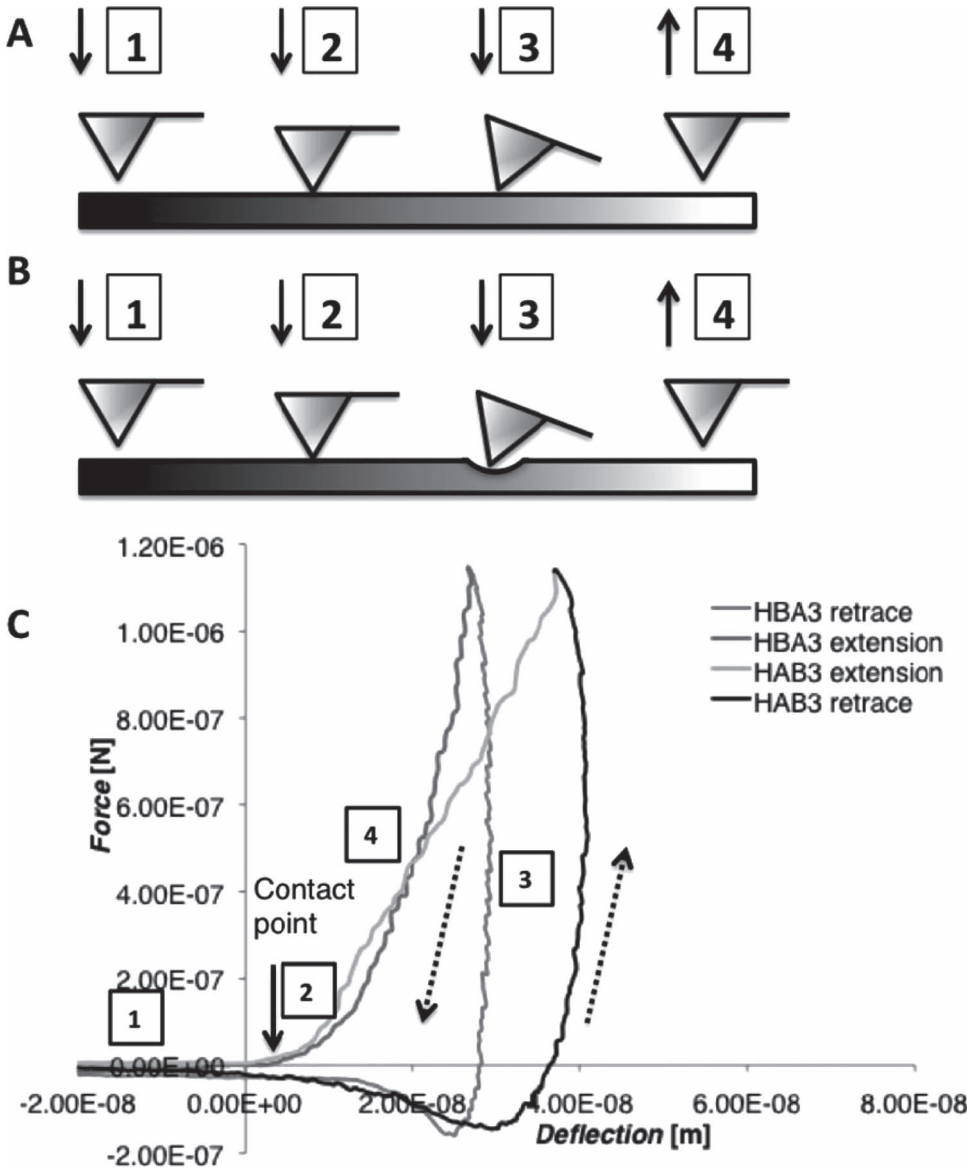

Figure 4. Schematic of AFM force measurement by indentation, for the case of A) stiff and B) soft surface. The numbers in this graph refer to the corresponding sequence in the force curves: 1) piezo is approaching to the surface; 2) the AFM tip is in contact with the surface (contact point); 3) piezo is further moving down, leading to the elastic indentation in the case of a soft surface; 4) piezo is moving up. C) Force curves of HBA_3 (red), HAB_3 (green). The arrows mark the contact point, the point where the cantilever first comes in contact with the sample surface. The trace and the retrace curves are also indicated by dashed arrows.

2.4. Force Curves and Young's Modulus

Nanoindentation was performed to obtain local mechanical properties represented as force-curves, which were later used to determine the Young's modulus for the spider silk-like block copolymer films. Typically, the cantilever tip was allowed to indent onto the polymer sample, resulting in a force curve that can be analyzed for elastic response of the sample to the small loading force applied to the tip (**Figure 4**). Elastic modulus was calculated using force and deflection values from Figure 4 and from theory.[31] Elastic moduli were determined as E_{HAB3} = 2.36 ± 0.84 GPa and E_{HBA3} = 2.86 ± 0.61 GPa for a total of 20 points for each film. Statistical analysis indicated a significant difference between the samples ($p < 0.05$). The slope of the curve gives a qualitative measure of elastic properties of the sample. For a stiff sample, the force curve was characterized by a flat area (Figure 4) when the tip was approaching the sample, and by a slope region where the cantilever deflection is identical to its vertical position. However in the case of soft samples HBA_3 and HAB_3, the slope becomes shallower as a result of a decrease in deflection value due to elastic indentation. Though both block copolymers are of similar molecular weight, their differences in elasticity were due to: a) primary sequence chemistry and b) the effect of water during film formation. We

assume that water permeates[32] into the amorphous matrix (here block B), thereby hydrating the amino acid chains interfering with the hydrogen bonding during film formation and leading to different assembly outcomes. The increased mobility and reduced intramolecular hydrogen bonding may be a reason for the lower Young's modulus for HAB_3 compared to HBA_3. Generally, increased β-sheet content leads to an increase in the elastic modulus, but decrease in elasticity.[33] Furthermore, the values of HBA_3 and HAB_3 were different than that of chimeric spider silk (1.1 GPa)[34] because the latter is comprised of polyalanine regions sandwiched between amorphous GGX regions, in comparison to a long stretch of polyalanine regions along with bone sialoprotein binding peptide. Values were similar to silk fibroin films (2.7 GPa),[35] but far from the values attributed by the major ampullate of *N. clavipes* (20–22 GPa).[36]

Protein size plays a key role in determining mechanical properties because of the intermolecular interactions and fewer protein chain ends (defects).[37] Elasticity of spider silk fibers has been determined by AFM spectroscopy by pulling[38] and contact modes.[31] Recombinant synthesis of native-sized spider silk constructs[39] displayed mechanical properties comparable to that of native spider silk. The reported recombinant fibers showed a modulus twice that of native spider silks, but tenacity was nearly four times lower due to the molecular weight. Comparable results were obtained when fibers were obtained by aqueous post spin stretching.[40] Thus, there remains a lot to be understood on how the silking process in spiders evolved to control chain assembly, to assess the role of the non-repetitive regions at the chain ends, and to control water content, along with issues of salts, ionic composition and pH during transit of the proteins through glands prior to spinning.[41–43]

2.5. Surface Morphology and Roughness

Topographical images were taken by AFM using tapping mode for both HBA_3 and HAB_3 at different scan sizes (20×20 μm^2, 5×5 μm^2 data not shown). When the surface features were assessed at higher resolution (10×10 μm^2 and 1×1 μm^2) noticeable differences were observed (**Figure 5**). Films formed from HBA_3 had surface features whereas HAB_3 appeared smooth, as detected by SEM analysis (Figure 3). At higher magnifications, HBA_3 formed globule-like structures while HAB_3 was relatively flat (Figure 5c,d). The resolution of the repetitive segmented or globular-like structures was limited by the cantilever tip size. A possible reason for this result is the effect of tip geometry during measurement. If the tip is larger than the surface features, then the surface appears flatter as a consequence

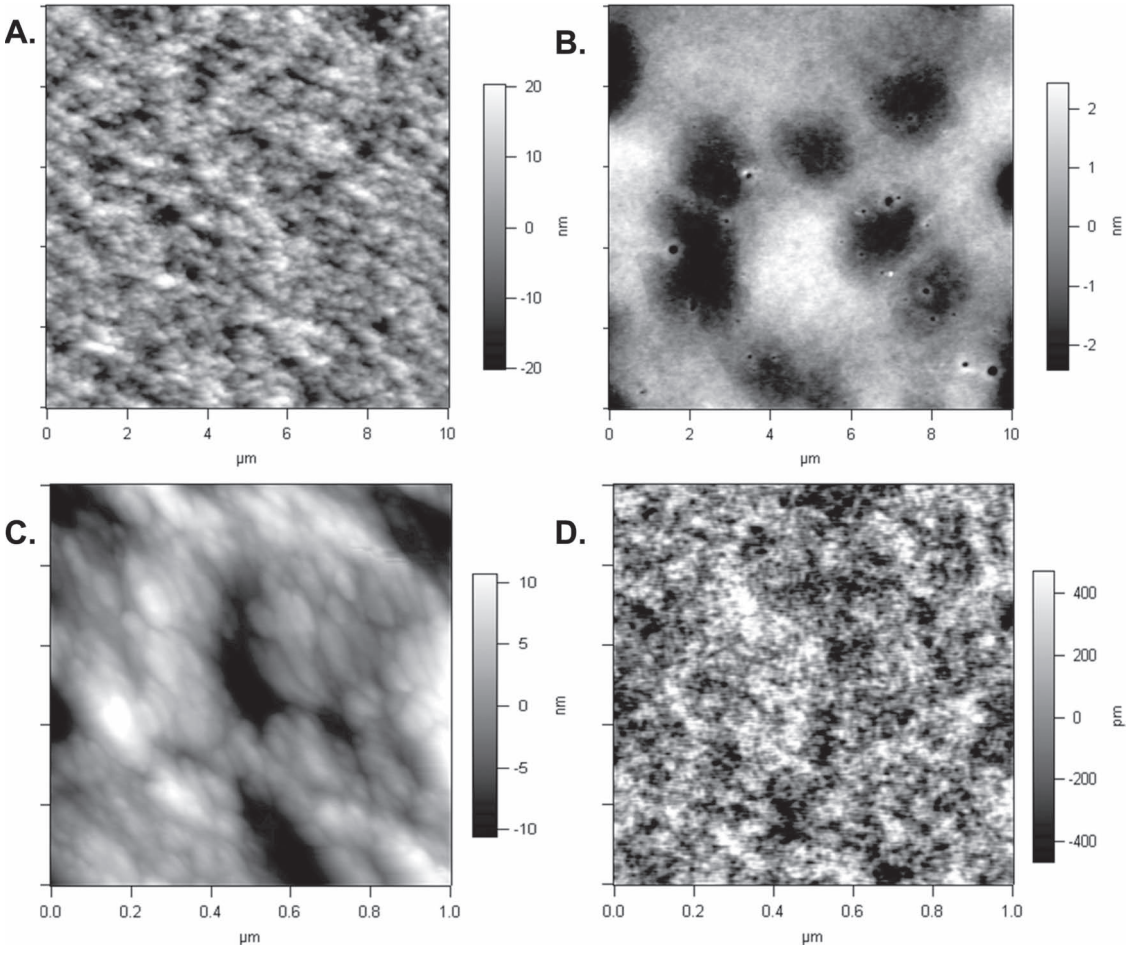

Figure 5. AFM height images of A,C) HBA_3 and B,D) HAB_3.

of poor contact points with the sample. In the case of HAB_3, occasional islands were observed on the film surface, which indicated some aggregation in the material while drying, however, the overall surface appeared flat. AFM topography of the dried films showed HAB_3 had a lower roughness of 1.21 nm and 0.236 nm at 10×10 μm^2 and 1×1 μm^2, respectively. With increasing polyalanine repeats, HBA_3 roughness was 7.41 nm and 4.87 nm at 10×10 μm^2 and 1×1 μm^2, respectively. The high surface roughness of the film may be attributed to structural rearrangement of the surface of the protein film by formation of β-sheets.

HBA_3 and HAB_3 have a net charge of –2 and 0 at pH 7.0, respectively. Since surface density is minimum for a polymer with no net charge, HAB_3 resulted in lower surface roughness. For HBA_3, the negative charges along with polyalanine domains have a propensity to form crystalline sheets and therefore responsible for the increase in surface roughness.

2.6. Contact Angle Measurements

The change in the overall hydrophobicities of the recombinant silk films on a mica substrate was quantified using contact angle measurements. When water was dropped onto the mica surface, it widely spread on the surface. In this situation, the goniometer could not measure its contact angle, suggesting extremely hydrophilic nature of the substrate. On the other hand, in the presence of recombinant proteins, water formed droplets with different contact angles, indicating the surface became hydrophobic. The contact angles were 40.2° ± 5.5° and 60.7° ± 4.0° for HAB_3 and HBA_3, respectively. The higher contact angle for HBA_3 is likely due to minimal molecular interaction of the protein with water droplet. Thus, differences in sequences have a dramatic influence on film properties, and variations in contact angle are consistent from roughness values obtained from AFM.

2.7 Enzymatic Degradation of Films

In order to show where crystalline regions are located, we performed additional studies using surface etching by enzymatic degradation of the films using α-chymotrypsin. Figure SI 2 (Supporting Information) shows morphology of degraded films in α-chymotrypsin at different time points (15 min and 1 h). From literature, α-chymotrypsin is incapable of digesting the crystalline β-sheets[44–46] and primarily catalyzes the hydrolysis of peptide bonds on the C-terminus of phenylalanine, tryptophan, tyrosine and leucine. The hydrophilic B block comprises of one tyrosine and two leucine residues and therefore is susceptible for cleavage to smaller fragments. Therefore, we should observe more degraded products for HAB_3 than for HBA_3. The degradation effects of silk fibroins[47] and Aβ fibrils[44,46] on treatment with protease XIV and α-chymotrypsin have been studied by analyzing changes in morphology with AFM. Enzymatic degradation of silk with protease XIV formed nanofilaments, whereas treatment with α-chymotrypsin did not significantly degrade silk indicating they were composed of crystalline elements, namely β-sheets. In the case of Aβ fibrils, protease XIV hydrolyzed the loop region linking the β-sheet regions inducing further degradation of β-hairpin structure resulting in spherical aggregates; whereas α-chymotrypsin unable to digest the loop and the protein retained its fibril-like morphology.

The control HAB_3 with buffer alone is shown in Fig SI 2a for reference, and forms uniform surface with occasional islands. After 15 min treatment with enzyme, the hydrophilic blocks were degraded easily in HAB_3 resulting in a mixture of fragments (Figure SI 2b, Supporting Information). Closer evaluation revealed nanoparticles on the order of ten to a few hundred nanometers, which formed due to the degradation of the hydrophilic regions and aggregation of the hydrophobic domains (Figure SI 3, Supporting Information). Degradation after an hour (Figure SI 2c, Supporting Information) indicated most of the surface is etched. HBA_3 with buffer alone as control also appeared to be uniform. It was interesting to observe similar morphology after 15 min treatment with enzyme (Figure SI 2d,e,Supporting Information). Higher magnification however showed some degradation products, but not to the extent observed with HAB_3 (Figure SI 3, Supporting Information). This indicated that the hydrophobic blocks were resistant to the enzyme and degraded at a slower rate. Treating films with enzyme for longer duration ultimately resulted in degradation products in both cases. α-Chymotrypsin is also reported to digest glycine, alanine, serine, threonine, valine as secondary cleavage sites.[48] Since the recombinant proteins consist primarily of these residues, secondary hydrolysis occurs at longer durations, results in degradation fragments. However, the results obtained at 15 min post treatment showed clear differences in terms of surface morphology and roughness.

The surface roughness was also determined. Under normal conditions, surface roughness of HAB_3 was lower than HBA_3. But, post-treatment with enzyme lead to an increased roughness. With respect to HBA_3, roughness remained almost the same (Table SI 1) indicative of the resistance of the recombinant protein to be degraded, denoting these regions are indeed hydrophobic (block A).

2.8. Mechanical Properties of Films

Both recombinant films were tested under water annealed condition alone and dry tests were not performed because of difficulties in handling the films for testing. The hydrophobic nature of HBA_3 film led it to break even before it could be tested. As a result, in order to better compare the films, water annealing (80% relative humidity, RH) was used for analysis. Moreover, these annealed films corresponded to the computational approach. The films displayed a qualitatively similar stress/strain behavior: toe region and a linearly increasing elastic-like portion (where the linear elastic modulus was extracted), followed by a plateau region that extended until eventual failure (where UTS and failure strain were extracted).

Post-hoc analysis revealed distinct differences between samples (**Table 2**). Surprisingly, annealed HAB_3 films had a higher modulus in the toe and linear region ($p < 0.05$) than HBA_3 films. Likewise, UTS was lower for HBA_3 in comparison to HAB_3. The elastic modulus of HBA_3 and HAB_3 were determined to be 161 and 553 MPa, respectively.

Table 2. Mechanical properties of water annealed recombinant silk films.

Code	Linear elastic modulus at 2–3% strain [MPa]	Ultimate tensile strength [MPa]	Failure strength [%]
HBA_3	161.9 ± 27.5	13 ± 0.7	43.8 ± 16.9
HAB_3	553 ± 31.3	20.9 ± 7	6.1 ± 3.4

Analysis of failure regime showed a failure strain of 43.8% for HBA_3 after exposure to humidity. The important role of water in altering the mechanical behavior of films has been exhibited in native silk due to disruption of interchain hydrogen bonding and swelling behavior of the amorphous regions in the film structure.[49] Indeed, hydration of HBA_3 decreases mechanical properties drastically because of the plasticizing effect of water. The presence of water vapor on cast films results in interactions via intermolecular forces, mostly hydrogen bonding. This interaction alters hydrophobic hydration states of the polymer chains because they are hydrophobic proteins due to high content of polyalanine repeats. During the process of elastic deformation, water molecules bound to the silk chains slip and reorient, allowing rearrangement of HBA_3 to assume a more thermodynamically stable state in the form of β-sheets. Due to absorption of water, there is an overall degree of molecular reorganization between the amorphous and crystalline domains of the film. Thus, in the dry testing state, the presence of β-sheet corresponds to film stiffness, whereas increased β-sheet correlates with increased water absorption which has a greater affect on increasing material ductility as opposed to promoting enhanced material strength. HAB_3 on the other hand, with fewer hydrophobic repeats was unable to reorient leading to failure at 6.1 %.

2.9 Mechanical Properties of Fibers

Unlike the films, increased β-sheet content for these fibers and non-fibrillar materials does not correlate to either increased strength nor extensibility. HBA_3 blend materials have little overall mechanical integrity and fall apart upon slight agitation. Mechanical testing via uniaxial loading to failure for HAB_3 blends was insightful, but yielded no quantitative data. These fibers, with diameters ranging from 5–10 μm, were incredibly brittle (even when wet), and broke immediately upon any load application without exhibiting any elongation. Thus force–extension plots (and resulting stress–strain plots) were flat lines without useful data for fiber modulus or strength. While the mechanisms of this failure are not fully understood, these results indicate that processing conditions (film drying vs. controlled spinning) greatly affect materials properties, and these conditions can be optimized (flow rates, pH, ion content, concentration) to produce beneficial differences in properties in future work.

2.10. Structure Convergence

Differences in the predicted secondary structures are evident during tempering and equilibration in molecular dynamics simulations, as visualized with cartoon representations in **Figure 6**a. While the lattice of each sequence begins equally extended, alanine-rich BA_3 forms more β-sheet structures and remains more extended during both tempering and equilibration. AB_3 contains less alanine and in turn forms fewer β-sheet structures and develops a nearly helical overall structure after equilibration. Convergence of each structure is considered sufficient due to the negligible rate of change of root-mean-square-deviation (RMSD) in Figure 6b as well as the total β-sheet content in Figure 6c after 10 ns of tempering (shaded area) followed by 10 ns of equilibration (unshaded area). While each lattice initially forms a high prevalence of extended conformations, the total β-sheet content of both structures decreases during tempering by escaping local trapping within the conformational energy landscape. The β-sheet content of both structures also decreased during equilibration as explicit water molecules diffused among the strands and disrupted unstable β-sheets. The overlapping polyalanine segments in BA_3 provided a local hydrophobicity that discouraged water-mediated disruption of β-sheets, and the equilibrated BA_3 structure maintained 39% β-sheet content. With fewer polyalanine segments, the equilibrated AB_3 structure maintains only 11% β-sheet content.

2.11. Pull-Out Testing

A correlation was observed between β-sheet content and mechanical behavior in the molecular dynamics simulations, seen visually in **Figure 7**a. Each structure exhibited three stages during deformation: extension of the protein, straightening of the two pulled central strands, and finally shearing and failure of the protein. While the BA_3 structure was not as extensible, the aligned arrays of hydrogen bonds among the β-sheets allowed higher shear strength, failing at 3.45 nN. The helical, amorphous geometry of the AB_3 structure allowed 1.5 times as much extension but failed at 2.40 nN, 70% the strength of BA_3. The three stages of deformation correlated to a change in β-sheet content and a change in stiffness, seen in Figure 7b. A characteristic valley in stiffness marks the beginning of the strain-hardening mechanism: a sudden increase in β-sheet content as strands are straightened and aligned. After the whole lamellar protein was extended, the loaded central strands straightened and additional β-sheets formed from these newly extended regions. The total β-sheet of BA_3 rose from 39% to 51%, and likewise for AB_3 from 11% to 26%. This increase in β-sheet content accompanied a stiffening behavior, seen in the shaded area in Figure 7b. As cross-sectional area and volume of the unit cell were difficult to define at the molecular scale in solvated conditions, stiffness is presented as a more convenient metric than engineering stress. Stiffness is here defined as the instantaneous slope of the force/length curves. Within the stiffening region, the stiffness of BA_3 increases from 0.03 N/m to 1.31 N/m, a 44.7-fold increase, and the protein failed catastrophically as the β-sheets shear. The stiffness of AB_3 from 0.04 N/m to 0.46 N/m, an 11.5-fold increase, and softened before failure as the random-coil strands slip. Both cases also show a coinciding sudden decrease in β-sheet content and stiffness immediately preceding failure as H-bond clusters were ruptured in shear.

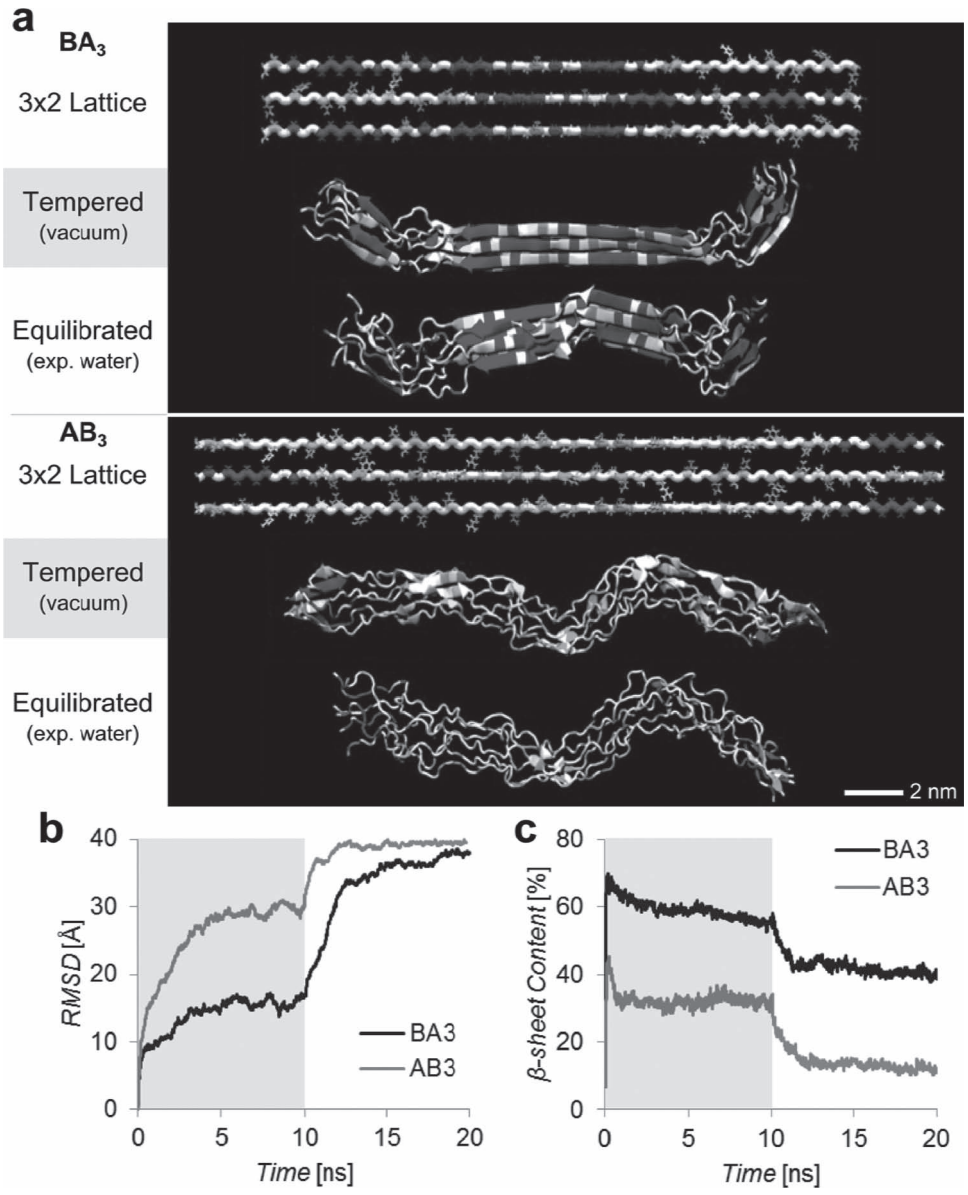

Figure 6. Molecular structure for each sequence considered. A) Length and secondary structure change is visible during tempering in vacuum and equilibration in explicit water. Here, explicit water is hidden for clarity, and residues are colored by name (alanine is blue). Convergence for each stage is determined by B) RMSD and C) changes in total β-sheet content.

3. Conclusions

The integration of biopolymer synthesis and processing with computational modeling was exploited here as a starting point to accelerate the design process for specific functional materials. Though time- and size-scales are different in experimental and computational approach, adopting similar boundary and environmental conditions resulted in a more complete description of the material behavior and predictive trends can be extracted from modeling reults. For films, both copolymers formed continuous surfaces. In addition to variations in surface roughness and mechanics, HBA_3 films had higher β–sheet content than HAB_3 as was predicted via simulations. Contact angle analysis also indicated HBA_3 was more hydrophobic than HAB_3, supporting roughness values obtained from AFM. However, from mechanical tests, HAB_3 had higher moduli than HBA_3 with HBA_3 having a strain failure greater than HAB_3. For fibers, HBA_3 could not be spun in to fibrous material via our microfluidic device, whereas HAB_3 could. The polyalanine rich HBA_3 material also formed significantly more β-sheets than the HAB_3 blend matching our modeling trends. We believe that differences in the absolute values for β-sheet content between experimental (films and fibers) and modeling are due to both large differences in the time scale of assembly (femto seconds for computation vs. seconds for fibers vs. hours for films) as well as removal of water and methanol during the spinning process. An increase in β-sheet content was observed from films to fibers (10.8 ± 3% for HAB_3 and 21.1 ± 5% for

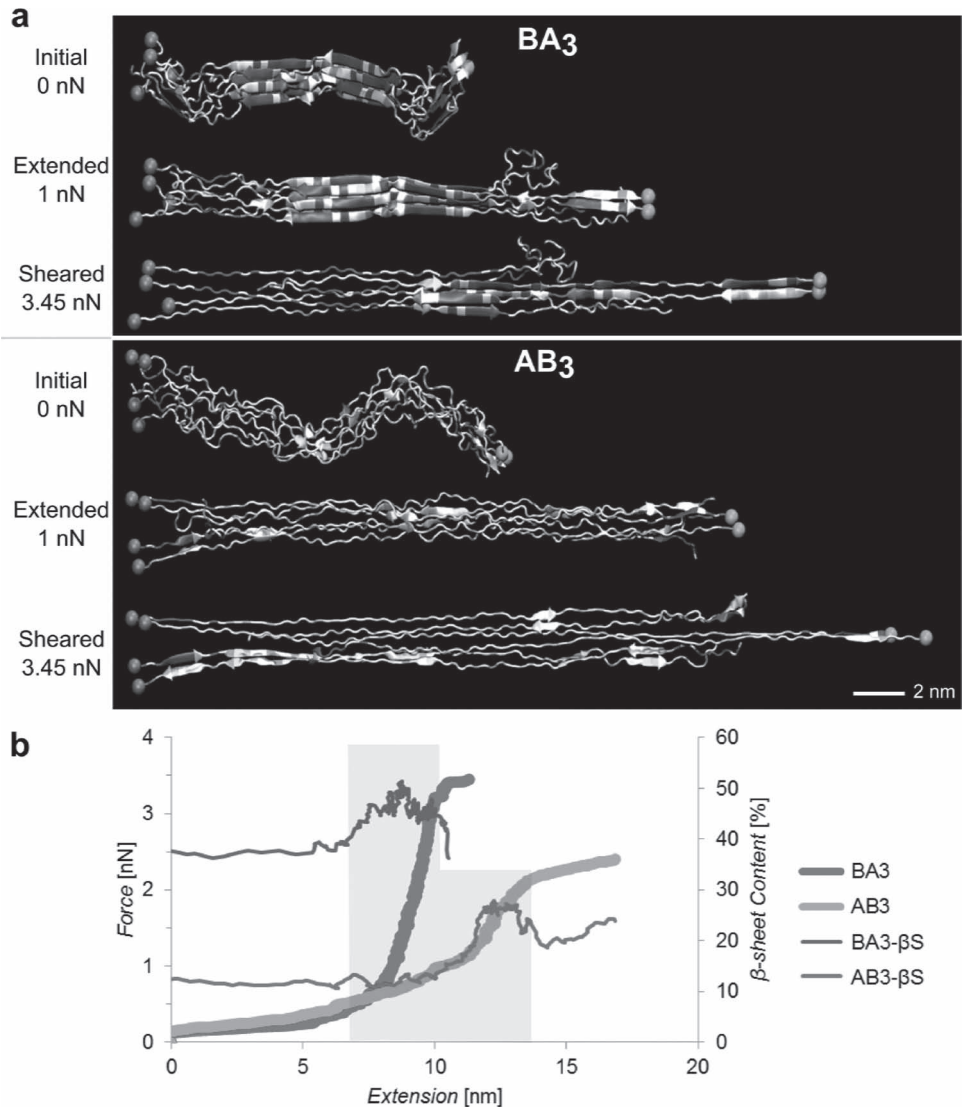

Figure 7. Force-control pullout testing of the equilibrated structures in explicit water. A) Extension and secondary structure change are visible during deformation. Here, explicit water is hidden for clarity, and residues are colored by name: alanine is blue, etc. B) Total instantaneous β-sheet content (thin line) is correlated with the force-extension curves (thick line) for each structure.

HBA_3 for films vs. 14.6 ± 5% for HAB_3 and 29.9 ± 2% for HBA_3 for fibers) which we believe can be attributed to protein strand elongation during flow in the device, and similar trends were seen during the protein extension phase in the pull-out model prior to failure. It should be noted that our current computational models predict the interaction of multiple recombinant peptide strands but do not include the RSF dope material. The interactions of these short protein strands (pure copolymer materials) were not sufficient to facilitate continuous fiber formation, so longer regenerated silk molecules were necessary to bridge between the structures formed by these peptides. However, simulating the assembly of such long proteins at sufficient time and length scales is beyond the current ability of atomistic molecular dynamics. While modeling the general assembly of tertiary and quaternary structures would indeed require larger scale techniques, e.g. coarse-grain mesoscale molecular dynamics, the atomistic scale simulations presented in this work serve to identify trends in secondary structure and hydrophobic packing among the domains that must be reflected in larger scale models. These trends from the atomistic-scale simulations, as well as considerations to account for processing conditions, are currently being included in a next-generation coarse grain model.

Our modeling results predict that HBA_3 will be more predisposed to form β-sheet structures than HAB_3, and experimental evidence supports this prediction. Given the previously established correlation between β-sheet content and organization and overall mechanical properties of native silks, this prediction would suggest that HBA_3 would form better and stronger fibers. However, the observed results show that this variant is not well suited to spinning in this device. The solution, even when mixed with regenerated silk, is viscous and difficult to

control in flow. Issues such as channel clogging had a much higher prevalence in attempts to spin HBA_3 than its less crystalline counterpart. When "spinning" was achieved and a product could be collected from the device, the fibers that had formed were entangled in non-fibrillar materials making it impossible to isolate fibers for characterization or use.

We believe that the HAB_3 copolymer is more suited to this spinning process because of its primarily semiamorphous structure, which allows it to easily for associations with other protein strands of both copolymer and RSF leading to a continuous fiber that is likely structurally similar to RSF fibers. The HBA_3 copolymer on the other hand is rich in polyalanine regions that are repetitive and tend to form β-sheet structures, and we believe that the copolymer strands are self-associating rather than forming the intermolecular structures that are necessary for fibers.

Overall, we have presented a three-pronged approach to tailored materials design in which each aspect of the process (sequence control, processing and modeling) facilitates a further understanding of the materials and also feeds into the others towards a more optimized or predictable materials outcome, in this case function. In this interative process, results from experimental successes and failures, along with modeling predictions, inform future material design, and with the accumulation of evidence this process will focus on optimized materials in a novel manner. We plan on exploring our scope by synthesizing additional generations of variants with alternating blocks to further understand the relationships that govern how these silk-mimetic polymers assemble.

4. Experimental Section

Expression and Purification of Recombinant Proteins: The construction, cloning, expression and purification of the spider silk-like block copolymers followed our previously published procedures.[25–27] The amino acid sequences of HBA_3 and HAB_3 was adapted from natural sequence of MaSp1 from *Nephila Clavipes*, comprising of block B (QGGYGGLGSQGSGRGGLGGQ) and block A (GAGAAAAAGGAG) resulting in a molecular mass of 10,068 and 11,967 Da, respectively. Briefly, the spider silk-like block copolymer genes were expressed in *E. coli* strain RY-3041, a mutant strain of *E. coli* BLR (DE3) defective in the expression of SlyD protein.[50] Cells were grown at 37 °C in LB medium to an OD_{600} of 0.6 at which point protein expression was induced with 1 mM IPTG (isopropyl-D-thiogalactoside; Fisher Scientific, Hampton, NH). The cells were harvested 4 h after induction by centrifugation at 10 000 g (Sorvall, Fisher Scientific, Hampton, NH). Purification of the proteins was performed under denaturing conditions using Ni-NTA resin (Qiagen, Valencia, CA) using the manufacturer's protocol.

Preparation of Films from Recombinant Proteins: HBA_3 was dissolved in 8 M urea or 6 M guanidinium thiocyante at 8% w/v and dialyzed extensively in water at 4 °C with exchanges every 3 h to obtain the polymer in solution. Due to differences in solubility, lyophilized HAB_3 was solubilized directly in water at a concentration of 8% w/v. Films were prepared on polydimethylsiloxane (PDMS) substrate by drop casting 50 µL of the samples and allowed to dry at room temperature and later peeled off when dry for structural analysis and SEM.

Processing of Regenerated Silk and Materials for Microfluidic Spinning: Regenerated silk fibroin (RSF) aqueous solution of 8% w/v and pH 6.6 was prepared from *Bombyx mori* cocoons according to a previously published protocol.[51] Poly(ethylene oxide) (PEO) aqueous solution of 3% w/v was prepared from 900 000 MW PEO (Sigma Aldrich, St. Louis, MO). Hydrochloric acid solution (1 M) (Sigma Aldrich, St. Louis, MO) was added to adjust the pH of the PEO solution to 1.5. The microfluidic devices were designed to mimic certain aspects of natural silk processing in a controlled manner and are fabricated from poly(dimethylsiloxane) (PDMS) (Sylgard 184, Dow Corning Corp., Midland, MI) as previously reported.[6] Spinning utilized hydrodynamic flow focusing to induce structural changes in the proteins and form fibers. Fibers were spun from mixtures of 70% silk-like recombinant copolymer and 30% regenerated silk solution (dope), collected from a methanol reservoir, washed multiple times and stored in water overnight before further analysis.

Secondary Structure Analysis: Since β-sheet and random coil/helix are considered important factors related to mechanical properties of recombinant silk, ATR-FTIR analysis was performed on the films to obtain secondary structure content of HBA_3 and HAB_3. For silk fibers, spectra were obtained from dried fiber bundles.Spectra were collected using a Jasco model FT/IR-6200 type A equipment (Jasco, MD) accessorized with MIRacleTM attenuated total reflection (ATR) Ge crystal cell in the absorption mode. For each measurement, 256 scans were recorded at a resolution of 8 cm^{-1} in the spectral region from 4000–400 cm^{-1}. The fractions of β-sheet, alpha helix and random coil were evaluated with Fourier self-deconvolution using OPUS 5.0 software[28] and quantified in the amide I region (1700–1600 cm^{-1}) and later normalized. OPUS deconvolution software was performed using a Lorentzian line shape with a half-bandwidth of 25 cm^{-1} and a noise reduction factor of 0.3. FSD spectra were used to curve fit to measure the relative areas for the amide I region components.

Atomic Force Microscopy: An Asylum Research MFP-3D-Bio Atomic Force Microscope (AFM) was used for imaging and force curve measurements. Surface topography was determined by using tapping mode, with a scanning range of 10 μm^2 and scanning rate of 1.0 Hz. A 100 µL sample of 4% w/v was deposited as a drop on a freshly cleaved mica substrate, and allowed to dry overnight and imaged. The heights of structures were determined by section analysis using IgorPro 6.22A image analysis software. The root-mean-square (rms) and the arithmetic average height (R_a) were determined using software to find differences between roughness of samples. Rms represents the standard deviation of the height values within a given area and allows the surface roughness to be determined by statistical methods. R_a is a frequently used roughness parameter and is defined as the average deviation of the roughness irregularities from the mean line over one sampling length. Force curves were obtained with AFM in the contact mode. Before conducting nanoindentation, spring constant of silicon cantilever (Asylum Research, AC160TS) was measured (k = 37.21 nN/nm) and measurements were performed as reported earlier[31] with sample dried on freshly cleaved mica substrate. A total of 20 curves were analyzed for both HBA_3 and HAB_3. Mica served as substrate surface whose elastic modulus was 160GPa.

Contact Angle: Water contact angles were measured on the drop casted films by means of contact angle goniometer (Model 250 G/T, Ramé Hart Instrument Co.). Contact angle (CA) was measured by adding 2 µL of Milli-Q water until largest contact angle was achieved without increasing the solid/liquid interfacial area. CA values of the left and right sides were measured, and an average value was used. All CA data were an average of three films each, with at least three measurements on different locations of the film.

Preparation and Analysis of Films by Enzymatic Degradation: The recombinant proteins (4 w/v) were drop casted on a pre-cleaned silicon wafer and allowed to dry overnight. Films were treated by proteolytic enzyme, α-chymotrypsin (Sigma-Aldrich) for 15 min and 1h in 0.1 M phosphate buffer solution (pH 7.4) at room temperature. The concentration of α-chymotrypsin was set to 10 µg/mL. After various time points, the surfaces were rinsed with de-ionized water and allowed to dry overnight. They were observed by Atomic Force Microscope (AFM, Nanoscope V, Veeco). Silicon cantilevers with spring constants of 3 N/m were used in tapping mode. Images were recorded in three different regions and values are mean of triplicate reading.

Mechanical Analysis of Films: Uniaxial tensile tests were performed on an Instron 3366 testing frame equipped with a 100 N capacity load cell as in.[52] A volume of 200 µL (4% w/v) recombinant spider silk solution was first cast on to rectangular PDMS (5 mm in width and 25 mm in length), and this substrate was used for drying off water. The volume of solution added to the PDMS substrate was chosen to optimize the overall

casting time and thickness uniformity based on prior casting studies.[52] The films were then left to dry slowly by covering with lid under ambient conditions. Once dried, samples were exposed to 80% relative humidity (RH) in order to allow removal from the PDMS substrate. The 25 mm samples were fixed between pneumatic clamps, leaving a 25 mm gage length, and a strain-control rate of 0.1% s^{-1} was specified while the sample was pulled to failure. The initial elastic modulus, yield stress, and tensile strength were calculated from stress/strain plots.[53] Data was replotted using a custom LabVIEW program, where the cross-section of 0.1 mm^2 was assumed, based on a sample width of 5 mm and nominal thickness of 20 μm as measured by SEM. This cross-section was used for the conversion to stress [MPa] and the gage length for each individual sample [mm] was used for calculation of strain. A linear elastic modulus was taken by using a best-fit line approximation within the range of 2–3% strain. The ultimate tensile stress (UTS) [MPa] was defined as the highest point of stress recorded during the test and the failure stress [%] was reported as the corresponding strain value at the point of UTS.

Fiber Mechanical Characterization: HAB_3 copolymer blend fiber mechanics were investigated via uniaxial tensile testing. Single fibers were mounted on to support frames and loaded on to an Instron. Fibers were extended at a rate of 0.01 mm/s until failure. Resulting force–elongation plots, along with fiber diameter and intial length, were used to calculate ultimate tensile strength and strain at failure. Non-fibrillar HBA_3 copolymer blend materials exhibited no mechanical integrity, and thus could not be analyzed via uniaxial tensile testing.

Computational Methods: The model systems treated here focus on the parallel and antiparallel aggregation of aligned BA_3 and AB_3 block copolymers. The poly histidine tag with the polylinker was excluded, as it was found to have unordered structure and did not play a role in structure formation.[54] We first simulate annealing to escape local energy trapping of the initial aligned lattice structure of copolymer strands. Experimental studies of recombinant silk[6,16] suggest that mechanical shear within a narrowing elongational flow extends and aligns silk protein strands during spinning, and that this encourages alanine "amyloidization" into extended nanoscale β-sheet crystals that cross-link a semiamorphous filament network (Figure 6a). Mimicking this process, an extended conformation is used when creating a single strand of each copolymer sequence unit using the TINKER Molecular Modeling Package with CHARMM-22 topology. A rectangular lattice structure (Figure 6b) is created by arranging two parallel layers, where each layer is made of three MaSp1 strands in an antiparallel arrangement in the side-chain direction. In this initial lattice structure, each strand is at a minimum distance of 10 Å to avoid geometric interference of the side-chains and to discourage local conformational energy trapping, as this distance is much larger than typical molecular interactions. While this simulation protocol is somewhat limited, as it does not account for all processes and reactions occurring during silk spinning,[55] the extended starting configuration mimics the elongational flow of the concentrated dope in the spinning duct and encourages alanine aggregation leading to crystal formation rather than folding of each strand upon itself.[16]

Simulated Annealing: To create an intermediate test structure from the initial lattice for both BA_3 and AB_3 sequences, we simulated each lattice with Langevin dynamics in vacuum using NAMD. Annealing in vacuum allows more of the conformational space to be explored without temperature limitations imposed by solvents, e.g., the vaporization of water. A time step of 2 fs was used by employing the SHAKE algorithm for hydrogen atoms. Solvent friction was added via a Langevin friction term that allows for high mobility and conformational sampling. Since force fields are generally parameterized for room temperature calculations, we used higher temperatures for fast conformational search and overcoming kinetic trapping, and then cooled the system to 300 K before further equilibration, as an approximation of previous work in the structure prediction of silk proteins using replica exchange molecular dynamics (REMD).[14] In particular, each system was annealed for a total of 10 ns: 1 ns linear ramping from 300 K to 650 K, 4 ns at 650K, 1 ns linear ramping to 300 K, and 4 ns at 300 K.

Explicit Solvent Equilibration: After annealing in vacuum, the resulting intermediate structures constituted the test model ensemble (Figure 6). To obtain more realistic molecular conformation and tertiary protein structures, each intermediate structure was equilibrated for 10 ns in a fully wrapping, periodic waterbox of TIP3P explicit solvent using NAMD. To prevent image interactions, i.e. interactions between the protein and the virtual copies of itself across the simulation box boundary, the waterbox pads the protein by at least 10 Å on all sides. Equilibration was performed with Langevin dynamics at 300 K and with particle mesh ewald (PME) electrostatics to more accurately capture solvent interactions.

Analysis Methods of Structure Predictions: The secondary structure content of each equilibrated structure was determined using the STRIDE algorithm built into the VMD Molecular Graphics Viewer[56] and customized.tcl scripts. The STRIDE algorithm holds an advantage over DSSP and other secondary structural algorithms by employing pattern recognition of statistically derived backbone dihedral angle information.[57] Propensity for certain secondary structures along each strand were predicted by analyzing each peptide sequence candidate in the Protein Plot window in MATLAB for local hydropathicity and total β-strand preference (TBP) properties. The definition of hydropathicity, as defined by Kyte and Doolittle,[58] is based on an index of relative hydrophobicity ranging from –4.5 to +4.5. The value for an individual amino acid is a weighted average of the normalized transfer free energy from water to vapor, the fraction of side-chains found 100% buried in a sample of nearly 1300 experimentally studied proteins, and the fraction of side-chains found 95% buried in the same sample. Amino acids with a negative hydropathicity are considered hydrophilic, those with a positive hydropathicity are hydrophobic, and those near zero are ambivalent. For an entered peptide sequence, the hydropathicity of an individual residue is a weighted average of the hydropathicities of adjacent residues within a sliding window. Thus, a hydrophobic segment reinforces its own hydrophobicity.

The total β-strand preference[59] is a relative index ranging between 0 and 2 based on observed residue contacts in strand-strand interactions instead of the dihedral angles of a single residue. This index adds clarification to the traditional four-state distinction in secondary structure (α-helix, β-strand, reverse turn, and random coil) by focusing on tertiary structure environments such as the assembly of β-strands into a β-sheet. Index values for each naturally occurring amino acid were determined for both antiparallel and parallel β-sheets in an experimental sampling of 30 proteins. In order to emphasize the predictions of both the hydropathicity index and the TBP index on β-sheet distribution within the BA_3 and AB_3 sequences, we multiply the values of both indices at each residue along the sequence. To predict the β-sheet content within the test lattice, these values are then superimposed with values corresponding to an adjacent antiparallel strand.

Nanomechanical Testing: Nanomechanical testing was performed on each equilibrated test structure with TIP3P explicit solvent. Each test is simulated at 300 K using the NAMD molecular modeling program and CHARMM-22 force field. To prevent the protein from interacting with its image across the periodic boundary after large deformation of the protein, the simulation box, with fully wrapping periodic boundary conditions, was kept larger than the expected deformed size, and pressure control was disabled. While some water molecules become gaseous during this type of simulation, it is verified that most of the water maintains a liquid state surrounding the protein. Particle mesh ewald (PME) electrostatics was employed to better capture solvent effects and solvent-mediated changes in secondary structure.

The pull-out test loads the β-sheet crystal in double shear and was chosen to better represent the probable loading conditions of a fringed micelle polycrystalline material, in which strands within a crystal diverge and connect to separate crystals further in the fibrillar network. Figure 7a shows a schematic of the pull-out test loading conditions: The termini alpha-carbons of 4 strands are fixed, while the termini of the remaining two central strands are loaded. The simulation was complete when the protein has failed in shear, i.e. when one or more loaded strands have separated from the main body. The force $F(t)$ on each loaded alpha-carbon terminus is increased by a step of 20 pN every 20 ps of equilibration.

Statistical Analysis: Average value of 20 measurements were performed for nanoindentation experiments. Statistical differences were determined by unpaired t-test with two tailed distribution and differences were considered

statistically significant at $p < 0.05$. The values in AFM experiment is expressed as means ± standard deviation. For mechanical test, sample sets ($n = 3$) were statistically analyzed by using paired student t-test analysis.

Supporting Information

Supporting Information is available from the Wiley Online Library or from the author.

Acknowledgements

SEM experiments were performed in part at the Center for Nanoscale Systems (CNS), a member of the National Nanotechnology Infrastructure Network (NNIN), which is supported by the National Science Foundation under NSF award no. ECS-0335765. CNS is part of Harvard University. T.K.S. acknowledges Daniel Rizzo for helping run nanoindentation experiments, James White for helpful advice, and Benjamin Partlow aiding in running the mechanical tests. The authors acknowledge use of Boston University's Biointerface Core Facility and Whitaker Microfabrication Center. The authors thank the NIH (EB002520), NSF (CBET 1067093) and HL72900), and the AFOSR for support of this research.

Received: February 21, 2012
Revised: May 25, 2012
Published online: August 13, 2012

[1] M. Grujicic, P. S. Glomski, B. Pandurangan, W. C. Bell, C. F. Yen, B. A. Cheeseman, *J. Mater. Sci.* **2011**, *46*, 4787.
[2] V. L. Brookes, R. J. Young, F. Vollrath, *J. Mater. Sci.* **2008**, *43*, 3728.
[3] G. Vunjak-Novakovic, P. H. G. Chao, S. Yodmuang, X. Q. Wang, L. Sun, D. L. Kaplan, *J. Biomed. Mater. Res. Part B* **2010**, *95B*, 84.
[4] K. Numata, J. Hamasaki, B. Subramanian, D. L. Kaplan, *J. Controlled Release* **2010**, *146*, 136.
[5] T. Scheibel, A. Lammel, M. Schwab, M. Hofer, G. Winter, *Biomaterials* **2011**, *32*, 2233.
[6] M. E. Kinahan, E. Filippidi, S. Köster, X. Hu, H. M. Evans, T. Pfohl, D. L. Kaplan, J. Wong, *Biomacromolecules* **2011**, *12*, 1504.
[7] S. T. Parker, P. Domachuk, J. Amsden, J. Bressner, J. A. Lewis, D. L. Kaplan, F. G. Omenetto, *Adv. Mater.* **2009**, *21*, 2411.
[8] M. Li, M. J. Mondrinos, M. R. Gandhi, F. K. Ko, A. S. Weiss, P. I. Lelkes, *Biomaterials* **2005**, *26*, 5999.
[9] S. Keten, M. J. Buehler, *Appl. Phy. Lett.* **2010**, *96*, 153701.
[10] J. D. van Beek, S. Hess, F. Vollrath, B. H. Meier, *Proc. Natl. Acad. Sci. USA* **2002**, *99*, 10266.
[11] S. Keten, Z. Xu, B. Ihle, M. Buehler, *Nat. Mater.* **2010**, *9*, 359.
[12] B. L. Thiel, K. B. Guess, C. Viney, *Biopolymers* **1997**, *41*, 703.
[13] T. Lefèvre, M. E. Rousseau, M. Pézolet, *Biophys. J.* **2007**, *92*, 2885.
[14] G. H. Bratzel, M. J. Buehler, *J. Mech. Behav. Biomed. Mater.* **2012**, *7*, 30.
[15] C. Dicko, F. Vollrath, J. M. Kenny, *Biomacromolecules* **2004**, *5*, 704.
[16] S. Rammensee, U. Slotta, T. Scheibel, A. R. Bausch, *Proc. Natl. Acad. Sci. USA* **2008**, *105*, 6590.
[17] M. C. Philip, A. F. Stephen, M. A. Auerbach, J. W. Song, D. L. Kaplan, W. W. Adams, R. E. Eby, D. Mahoney, D. L. Vezie, *Polym. Adv. Technol.* **1994**, *5*, 401.
[18] S. W. Cranford, A. Tarakanova, N. Pugno, M. J. Buehler, *Nature* **2012**, *482*, 72.
[19] J. Kummerlen, J. D. vanBeek, F. Vollrath, B. H. Meier, *Macromolecules* **1996**, *29*, 2920.
[20] G. P. Holland, M. S. Creager, J. E. Jenkins, R. V. Lewis, J. L. Yarger, *J. Am. Chem. Soc.* **2008**, *130*, 9871.
[21] M. B. Hinman, R. V. Lewis, *J. Biol. Chem.* **1992**, *267*, 19320.
[22] R. Lewis, *Chem. Rev.* **2006**, *106*, 3762.
[23] N. A. Ayoub, J. E. Garb, R. M. Tinghitella, M. A. Collin, C. Y. Hayashi, *PLoS ONE* **2007**, *2*, 514.
[24] C. Y. Hayashi, N. H. Shipley, R. V. Lewis, *Int. J. Biol. Macromol.* **1999**, *24*, 271.
[25] O. S. Rabotyagova, P. Cebe, D. L. Kaplan, *Biomacromolecules* **2009**, *10*, 229.
[26] O. S. Rabotyagova, P. Cebe, D. L. Kaplan, *Macromol. Biosci.* **2010**, *10*, 49.
[27] S. T. Krishnaji, W. W. Huang, O. Rabotyagova, E. Kharlampieva, I. Choi, R. Naik, P. Cebe, V. V. Tsukruk, D. L. Kaplan, *Langmuir* **2011**, *27*, 1000.
[28] W. W. Huang, S. T. Krishnaji, X. Hu, D. Kaplan, P. Cebe, *Macromolecules* **2011**, *44*, 5299.
[29] X. Hu, D. L. Kaplan, P. Cebe, *Macromolecules* **2006**, *39*, 6161.
[30] Q. Lu, X. Hu, X. Wang, J. A. Kluge, S. Lu, P. Cebe, D. L. Kaplan, *Acta Biomater.* **2010**, *6*, 1380.
[31] A. Schäfer, T. Vehoff, A. Glisović, T. Salditt, *Eur. Biophys. J.* **2008**, *37*, 197.
[32] F. I. Bell, I. J. McEwen, C. Viney, *Nature* **2002**, *416*, 37.
[33] A. Nova, S. Keten, N. Pugno, A. Redaelli, M. J. Buehler, *Nano Lett.* **2010**, *10*, 2626.
[34] R. L. Reis, S. Gomes, K. Numata, I. B. Leonor, J. F. Mano, D. L. Kapan, *Biomacromolecules* **2011**, *12*, 1675.
[35] J. Yin, E. Chen, D. Porter, Z. Shao, *Biomacromolecules* **2010**, *11*, 2890.
[36] J. M. Gosline, P. A. Guerette, C. S. Ortleepp, K. N. Savage, *J. Exp. Biol.* **1999**, *202*, 3295.
[37] V. Renugopalakrishnan, R. V. Lewis, *Bionanotechnology: Proteins to Nanodevices*, 1st ed., Springer, Dordrecht, The Netherlands **2006**.
[38] N. Becker, E. Oroudjev, S. Mutz, J. P. Cleveland, P. K. Hansma, C. Y. Hayashi, D. E. Makarov, H. G. Hansma, *Nat. Mater.* **2003**, *2*, 278.
[39] X. X. Xia, Z. Qian, C. S. Ki, Y. H. Park, D. L. Kaplan, S. Y. Lee, *Proc. Natl. Acad. Sci. USA* **2010**, *107*, 14059.
[40] B. An, M. B. Hinman, G. P. Holland, J. L. Yarger, R. L. Lewis, *Biomacromolecules* **2011**, *12*, 2375.
[41] F. Vollrath, D. P. Knight, *Nature* **2001**, *410*, 541.
[42] F. Hagn, L. Eisoldt, J. G. Hardym, C. Vendrely, M. Coles, *Nature* **2010**, *465*, 239.
[43] G. Askarieh, M. Hedhammar, K. Nording, A. Saenz, C. Casals, *Nature* **2010**, *465*, 236.
[44] B. Lotz, A. Gonthier-Vassal, A. Brack, J. Magoshi, *J. Mol. Biol.* **1982**, *156*, 345.
[45] M. Li, M. Ogiso, N. Minoura, *Biomaterials* **2003**, *24*.
[46] K. Numata, P. Cebe, D. L. Kaplan, *Biomaterials* **2010**, *10*, 2969.
[47] K. Numata, D. L. Kapan, *Biochemistry* **2010**, *15*, 3254.
[48] M. M. Burrell, *Enzymes of Molecular Biology*, Vol. *16*, Humana Press, Totowa, NJ **1993**.
[49] J. Perez-Rigueiro, C. Viney, J. Llorca, M. Elices, *Polymer* **2000**, *41*, 8433.
[50] E. Bini, C. W. P. Foo, J. Huang, V. Karageorgiou, B. Kitchel, D. L. Kaplan, *Biomacromolecules* **2006**, *7*, 3139.
[51] H. J. Jin, S. V. Fridrikh, G. C. Rutledge, D. L. Kaplan, *Biomacromolecules* **2002**, *3*, 1233.
[52] B. D. Lawrence, F. Omenetto, K. Chui, D. L. Kaplan, *J. Mater. Sci.* **2008**, 6967.
[53] B. D. Lawrence, S. Wharram, J. A. Kluge, G. G. Leisk, F. G. Omenetto, M. I. Rosenblatt, D. L. Kaplan, *Macromol. Biosci.* **2010**, *10*, 393.
[54] C. R. Grace, M. H. Perrin, M. R. DiGruccio, C. L. Miller, J. E. Rivier, W. W. Vale, R. Riek, *Proc. Natl. Acad. Sci. USA* **2004**, *101*, 12836.
[55] L. Eisoldt, J. G. Hardy, M. Heim, T. R. Scheibel, *J. Struct. Biol.* **2010**, *170*, 413.
[56] W. Humphrey, A. Dalke, K. Schulten, *J. Mol. Graphics* **1996**, *14*, 33.
[57] D. Frishman, P. Argos, *Proteins: Struct., Funct., and Bioinf.* **1995**, *23*, 566.
[58] J. Kyte, R. F. Doolittle, *J. Mol. Biol.* **1982**, *157*, 105.
[59] S. Lifson, C. Sander, *Nature* **1979**, *282*, 109.